International Journal of Heat and Mass Transfer 52 (2009) 3790–3798

Contents lists available at ScienceDirect

International Journal of Heat and Mass Transfer

journal homepage: www.elsevier.com/locate/ijhmt

The effects of Prandtl number on wavy weld boundary

P.S. Wei [a,*], J.S. Yeh [a], C.N. Ting [a], T. DebRoy [b], F.K. Chung [c], C.L. Lin [a]

[a] Department of Mechanical and Electro-Mechanical Engineering, National Sun Yat-Sen University, Kaohsiung, Taiwan, ROC
[b] Department of Materials Science and Engineering, The Pennsylvania State University, University Park, PA 16802, USA
[c] Department of Mold and Die Engineering, National Kaohsiung University of Applied Sciences, Kaohsiung, Taiwan, ROC

ARTICLE INFO

Article history:
Received 23 August 2008
Received in revised form 19 February 2009
Accepted 19 February 2009
Available online 6 April 2009

Keywords:
Welding
Melting
Marangoni flow
Prandtl number
Thermocapillary flow
Fusion zone shape

ABSTRACT

The effects of Prandtl number on two-dimensional thermocapillary convection and molten pool shape induced by negative surface tension coefficient in welding or melting with a time-dependent and distributed incident flux are numerically predicted in this study. This work is also applicable for predicting the quasi-steady three-dimensional thermocapillary convection. In this model, the time-dependent incident flux is specified as a function of scanning speed and energy distribution parameter. The computed flow patterns and molten pool shapes under the flat free surface are found to have distinct regions for different Marangoni and Prandtl numbers. Prandtl number indicates the thickness ratio between momentum and thermal boundary layers, whereas Marangoni number with negative surface tension coefficient induces an outward surface flow. Rather than the enhanced pool depth resulted from melting from an induced vortex cell near the bottom in the case of Prandtl number much less than unity, the molten pool shape for Prandtl number much greater than unity can produce a thin and narrow edge. The variations of Peclet number and dimensionless beam power with flow and temperature fields and fusion zone shapes are similar. The dimensionless peak surface speed versus product of Marangoni and Prandtl number, which involve predicted peak speed and temperature and molten pool width on the surface, agree with scale analysis and experimental data provided in the literature.

1. Introduction

Heat transfer and fluid flow calculations in fusion welding has provided significant insight about the welding process and the welded materials. In simple alloy systems, the computed temperature fields can be used to model phase composition, grain structure and inclusion structure [1–4]. In many cases, the weld cross-sections show wavy fusion boundary where the slope of the fusion boundary changes sign depending on the location [4,5]. Previous research has established the importance of wavy fusion boundary in affecting the solidification process and the structure and properties of the welds. For example, Liu and DuPont [5] showed that the shape of the fusion boundary and the welding velocity affected the local dendrite growth velocity during welding of single-crystal nickel based superalloy. However, the conditions for the formation of such boundary have not been systematically understood. Computational heat transfer and fluid flow can also be used to compute weld pool geometry [6–11], cooling rate [7,10,11], local solidification rates, changes in alloy composition due to vaporization of alloying elements and dissolution of gases [12], and required to understand the defects such as ripping, humping, spiking, undercut and porosity [13–20].

Extensive three-dimensional computations have been first provided by Kou and Wang [6]. They presented a steady-state three-dimensional model to predict the effects of surface tension gradients (and buoyancy and electromagnetic forces) on flow and temperature fields, molten pool shapes, segregation and porosity during arc welding of aluminum. The computed results confirmed the finding on the role of surface tension gradient in weld pool convection and shape from Heiple and Roper [21]. Zacharia et al. [9] also developed an elaborate unsteady three-dimensional turbulent model accounting for surface tension coefficient affected by surface active solutes on fluid flow and temperature field and during arc and laser beam welding of type 304 stainless steel. Two cells were seen to be resulted from changing sign of surface tension coefficient in the presence of the surface active solutes near the edge of the pool.

Chan et al. [10] proposed a two-dimensional transient semi-infinite model to predict thermal and flow fields in a laser melted pool driven by thermocapillary force with negative surface tension coefficient. The heat source is stationary, even though the scanning speed and width of the source with constant flux were incorporated to non-dimensionalize time, space, momentum, and temperature. Neglecting latent heat and considering identical thermal conductivities between solid and liquid, it showed that there existed two counter rotating cells, except for high Prandtl number greater than 2.6 leading to the only cell induced the maximum

* Corresponding author. Tel.: +886 7 5254050; fax: +886 7 5254214.
E-mail address: pswei@mail.nsysu.edu.tw (P.S. Wei).

0017-9310/$ - see front matter © 2009 Elsevier Ltd. All rights reserved.
doi:10.1016/j.ijheatmasstransfer.2009.02.020

Nomenclature

f	volumetric fraction of liquid to solid
Fr	Froude number = $U/\sqrt{g\sigma}$
h	molten pool depth at the centerline, $h^* = h/\sigma$
$h_{s\ell}$	latent heat for solid–liquid phase transition
k	thermal conductivity ratio, $k^* = k/k_\ell$
Ma	Marangoni number, $Ma \equiv \lvert d\gamma/dT\rvert(T_m - T_\infty)\sigma/\mu\alpha_\ell$
Ma_f	Marangoni number, $Ma_f \equiv \lvert d\gamma/dT\rvert(T_{\max} - T_m)w/\mu\alpha_\ell$
p	pressure, $p^* = p/\rho U^2$
Pe	Peclet number = $U\sigma/\alpha_\ell$
Q	beam power, $Q^* = Q/[k_\ell\sigma(T_m - T_\infty)]$
Ste	Stefan number = $c_{ps}(T_m$-$T_\infty)/h_{s\ell}$
t	time, $t^* = tU/\sigma$
T	temperature,$T^* = (T - T_\infty)/(T_m - T_\infty)$
U	scanning speed
u,v	horizontal and vertical components of velocity, $u^* = u/U$, $v^* = v/U$
w	molten pool width, $w^* = w/\sigma$
X^*	half width of incident flux on top surface, $X^* = X/\sigma$
x,y,z	coordinate, as illustrated in Fig. 1, $x^* = x/\sigma$, $y^* = y/\sigma$, $z^* = z/\sigma$

Subscripts

f	free surface
ℓ	liquid
m	melting
s	solid
$*$	dimensionless quantity
∞	ambient

Greek letters

α	thermal diffusivity
β	thermal expansion coefficient, $\beta^* = \beta(T_m - T_\infty)$
γ	surface tension, surface tension coefficient $d\gamma/dT$ is constant
σ	energy distribution parameter
μ	dynamic viscosity

depth away from the symmetric axis. It seems questionable that the surface temperature increased with increasing surface tension parameter. The width-to-depth depth ratio increased with Prandtl number. It was interestingly found that the width-to-depth ratio increased with surface tension number until a local maximum around 9.8 was reached at the surface tension number around 55,000 for a Prandtl number $Pr = 0.1$. A further increasing surface tension number from 55,000 to 100,000 leaded to the width-to-depth ratio decreasing from 9.8 to 7.5 as a result of the deep penetration.

Limmaneevichitr and Kou [22] conducted experiments to explain the effects of Prandtl number and Peclet number on the weld pool shapes for gallium (Ga) and sodium nitrate ($NaNO_3$) subject to a stationary defocused CO_2 laser beam. In view of having low and high Prandtl numbers, metal Ga and $NaNO_3$ pools represented the low and high extremes of Peclet number, respectively, with commonly welded metals such as aluminum, steel and stainless steel falling in between. The Peclet number was defined by the product of maximum surface speed and radius of the pool divided by thermal diffusivity, indicating the ratio between heat transport by convection to that of conduction. Even though estimation of Peclet number is difficult due to the unknown maximum surface speed and molten pool width, it was indeed found that the pool bottom was concave for metal Ga with low Peclet number due to a promoted conduction down into the pool. For sodium nitrate $NaNO_3$, however, promoted outward convective heat transport, and the resultant pool bottom was shallow and flat. Reducing the beam diameter further increased surface speed and Peclet number. The fast outward surface flow turned and penetrated downward at the pool edge, resulting in a convex pool bottom. It was proposed that, the pool bottom convexity increases with increasing Peclet number.

In this study, the previous unsteady two-dimensional heat transfer model [23,24] is used to predict the fusion zone shape affected by Marangoni convection with a negative surface tension coefficient for different Prandtl numbers during melting and welding with a low-power density-beam. The heat source is a time-dependent function of energy distribution parameter and scanning speed. Even though the transport phenomena have been extensively studied, the wavy pool boundary affected by different Marangoni and Prandtl numbers is still required. Microstructures and defects of materials which are closely related to the wavy pool boundary encountered in materials and manufacturing processing can therefore be revealed from this work.

2. System model and analysis

In this work, an unsteady two-dimensional model [23,24] is used to simulate Marangoni convection during welding or melting of workpieces in depth H and width $B/2$. In reality, welding is a three-dimensional process, accomplished by an energy beam with a beam radius or energy distribution parameter σ moving at a scanning speed U along the joint plane in the negative z coordinate, as sketched in Fig. 1(a). The energy distribution parameter defines the region in which 95 percent of the total energy is deposited. Fluid flow in the molten pool is driven by thermocapillary force on the flat free surface at a cross-section $z = 0$, as illustrated in Fig. 1(b). To simplify the analysis without loss of generality, the major assumptions made are the following:

1. An unsteady two-dimensional heat transfer model subject to time-dependent incident flux is applied to simulate the quasi-steady three-dimensional heat transfer, as verified from scale analysis [25]. This is because the energy required for development of the two-dimensional fusion zone shape is of the same magnitude as that for heating and melting the incoming solid in the three-dimensional case.
2. Incident flux of energy beam absorbed by the top surface is of a Gaussian distribution, being relevant in laser and electron beam welding [26,27].
3. Electromagnetic forces are not accounted for, because the heat source is chosen as laser or electron beam.
4. The free surface of the pool is flat, due to a small capillary number ($\equiv \Delta T(d\gamma/dT)/\gamma_m$) around 0.05–0.1 in most metals [28].
5. Evaporation rates are neglected [12,29].
6. Physical and thermal properties are averaged within the temperature range considered.

With the above assumptions, dimensionless equations of continuity, momentum and energy in the workpiece are, respectively, reduced to

$$\frac{\partial u^*}{\partial x^*} + \frac{\partial v^*}{\partial y^*} = 0 \tag{1}$$

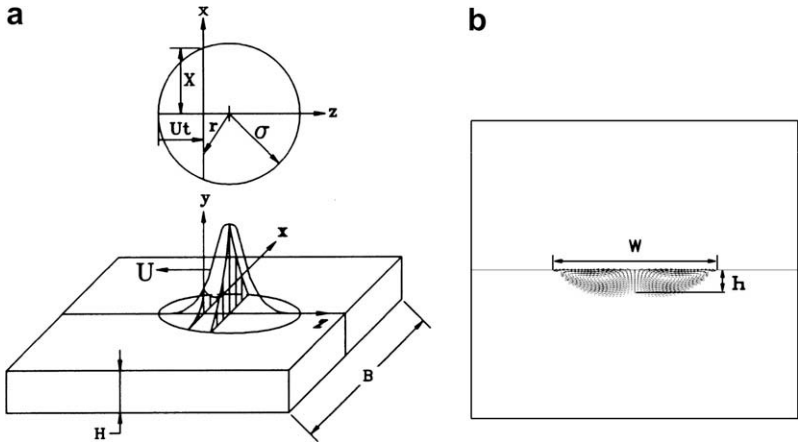

Fig. 1. Schematic sketch for (a) physical model and coordinates, and (b) computed results on the transverse cross-section at $z = 0$.

$$\frac{\partial u^*}{\partial t^*}+\frac{\partial u^{*2}}{\partial x^*}+\frac{\partial u^* v^*}{\partial y^*}=-\frac{\partial p^*}{\partial x^*}+\frac{Pr}{Pe}\left[\frac{\partial}{\partial x^*}\left(2\frac{\partial u^*}{\partial x^*}\right)+\frac{\partial}{\partial y^*}\left(\frac{\partial u^*}{\partial y^*}+\frac{\partial v^*}{\partial x^*}\right)\right] \tag{2}$$

$$\frac{\partial v^*}{\partial t^*}+\frac{\partial u^* v^*}{\partial x^*}+\frac{\partial v^{*2}}{\partial y^*}=-\frac{\partial p^*}{\partial y^*}+\frac{Pr}{Pe}\left[\frac{\partial}{\partial y^*}\left(2\frac{\partial v^*}{\partial y^*}\right)+\frac{\partial}{\partial x^*}\left(\frac{\partial u^*}{\partial y^*}+\frac{\partial v^*}{\partial x^*}\right)\right]-\frac{1}{Fr^2}[1-\beta^*(T^*-1)] \tag{3}$$

$$\frac{\partial T^*}{\partial t^*}+\frac{\partial u^* T^*}{\partial x^*}+\frac{\partial v^* T^*}{\partial y^*}-\frac{1}{Pe}\left(\frac{\partial^2 T^*}{\partial x^{*2}}+\frac{\partial^2 T^*}{\partial y^{*2}}\right)=-\frac{1}{Ste}\frac{\partial f}{\partial t^*} \tag{4}$$

where the term on the right-hand side of Eq. (4) represents latent heat evolution. The major driving force is Marangoni force, which is balanced by viscous stress on the flat free surface

$$\frac{\partial u^*}{\partial y^*}=\frac{-Ma}{Pe}\frac{\partial T^*}{\partial x^*} \tag{5}$$

The incident flux of a Gaussian distribution on the top surface is

$$\frac{\partial T^*}{\partial y^*}=\frac{3Q^*}{\pi}\exp(-3r^{*2}) \qquad \text{for} \begin{cases} |x^*| \le X^*(t^*) \\ 0 \le t^* \le 2 \end{cases} \tag{6}$$

where dimensionless radial coordinate and time-dependent half width of the incident flux are geometrically found to be (see Fig. 1(a))

$$r^*(t^*)=\sqrt{x^{*2}+(1-t^*)^2} \tag{7}$$

$$X^*(t^*)=\sqrt{1-(1-t^*)^2} \tag{8}$$

Dimensionless half beam width of the incident flux and time in Eq. (8) are, respectively, normalized by the energy distribution parameter, and ratio between the energy distribution parameter and scanning speed. The time-dependent beam radius governed by Eq. (8) therefore realistically accounts for the effects of scanning speed of energy beam on heat transfer in the two-dimensional model. The incident flux with time-dependent beam radius $X^*(t^*)$ is equivalent to that of the moving energy beam with a constant energy distribution parameter σ in the realistic three-dimensional case. Eqs. (6)–(8) indicate that the cross-section considered at $z^* = 0$ is irradiated by incident energy flux on a surface region $|x^*| \le X^*(t^*)$ and dimensionless time $0 \le t^* \le 2$. At dimensionless time $t^* = 0$, corresponding to zero half beam width, the incident energy starts to heat at $x^* = 0$ on the cross-section at $z^* = 0$. This can be considered as the moving energy beam starts to touch the cross-section. The half width of the incident flux increases from zero to the energy distribution parameter as dimensionless time increases from zero to $t^* = 1$. In order words, the beam approaches and leaves the cross-section after dimensionless time of zero and unity, respectively. A further increase in time results in the beam width to decrease. After $t^* = 2$, beam width becomes zero and no incident energy is irradiated on the top surface of the cross-section. Boundary conditions are zero velocities, and conduction balanced by convection on the right, left, and bottom surfaces. Initial conditions are $T^* = T_0^*$, $u^* = v^* = 0$.

2.1. Numerical procedure

A control-volume formulation and a fully implicit, staggered, finite-difference method was used to solve Eqs. (1)–(4) together with boundary and initial conditions [23,24]. Different mesh systems 90×90, 120×120, 180×180 for spatial coordinates, and mesh systems of 40 and 80 in the time direction within the total dimensionless time of 2.4 were used for testing convergence. The predicted dimensionless surface speed and temperature as functions of time for different meshes are found to converge, as shown in Fig. 2(a). In the case of the mesh system of $180 \times 180 \times 40$ used in this work, the relative errors of velocity and pressure became smaller than 10^{-4}. The maximum dilatation of the continuity equation was 10^{-5}. The relative errors for the sensible heat and fraction of liquid were less than 10^{-3} and 10^{-4}, respectively. In order to confirm the computed results, the predicted dimensionless peak surface velocity versus product of Marangoni and Prandtl numbers, which involve predicted peak velocity (u_f), temperature and molten pool width on the surface, is compared with that obtained from scale analysis for Prandtl number greater than unity [30,31], as shown in Fig. 2(b). It can be seen that the computed results agree with scale analysis. In welding or melting Marangoni number is as high as 10^3–10^4 for most metals, based on a surface liquid velocity 1–10 m/s, beam radius of 10^{-3}–10^{-4} m and thermal diffusivity of 10^{-5} m^2/s. Inertia and viscous forces must be of the same order of magnitude in the thin momentum shear layer. Furthermore, viscous shear is balanced by the driving force of thermocapillary force at the free surface. Irrespective of Prandtl number, the peak surface velocity can be scaled to be proportional to the 2/3 power of Marangoni number and 1/3 power of Prandtl number. Different scales for high Maragnoni number as discussed by Rivas and Ostrach [32] were due to scaling temperature difference involving further scaling of thermal boundary layer thickness. Rivas and Ostrach [32] also found that the weld pools predicted from this scale analysis agreed well with experimental data. Fig. 2(c) shows that the predicted dimensionless peak surface velocity versus product of Marangoni and Prandtl numbers agree with the same scale

analysis, and experimental data [33–35] for Prandtl number small than unity.

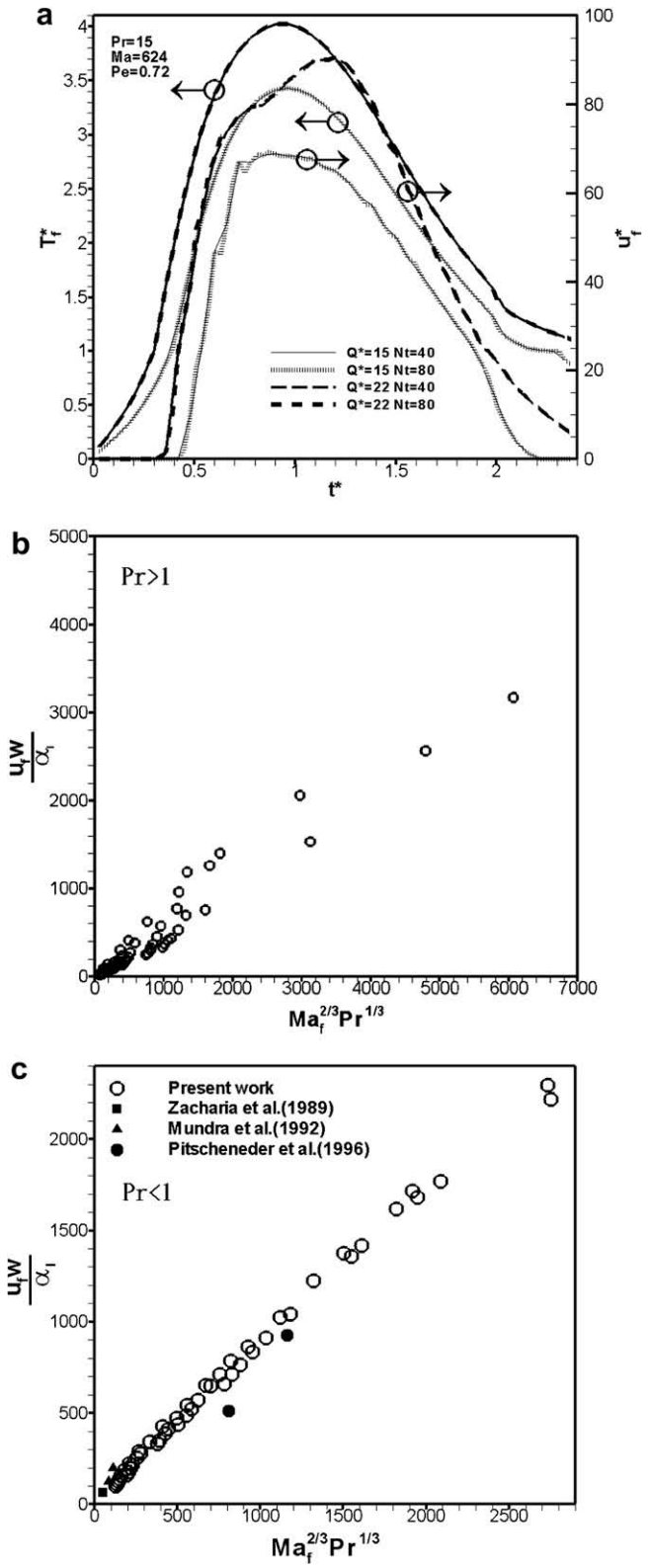

Fig. 2. (a) Convergence test for dimensionless peak surface temperature and velocity as functions of time, (b) comparison between predicted dimensionless peak surface velocity versus product of Marangoni and Prandtl numbers and scale analysis for Prandtl number greater than unity, and (c) comparison between predicted dimensionless peak surface velocity versus product of Marangoni and Prandtl numbers and scale analysis, and available experimental data [33–35] for Prandtl number less than unity.

3. Results and discussion

In this work, independent parameters primarily controlling physical phenomena are Marangoni number (Ma or Ma_f), Prandtl number (Pr), dimensionless beam power (Q^*) and Peclet number (Pe). Even though materials with high Prandtl number in welding or melting are rarely found, studying the effects of large Prandtl number on transport processes in this work has its academic importance and fundamental clarification of physical concepts. The effects of surface tension coefficient is included in Marangoni number, whereas the scanning speed and power of the incident flux are, respectively, accounted from Peclet number and dimensionless beam power. Rather than that defined by Limmaneevichitr and Kou [22], Peclet number defined by the product of scanning speed and energy distribution parameter divided by thermal diffusivity of the liquid indicates the ratio between scanning speed and diffusion rate of the incident flux. The following figures are referred to the transport phenomena and molten pool shapes corresponding to the time at which the molten pool area reaches the maximum.

The flow patterns for different Marangoni and Prandtl numbers are shown in Fig. 3(a). In the typical case of dimensionless beam power $Q^* = 15$ and Peclet number $Pe = 0.72$, the flow patterns and molten pool shapes can be classified into distinct regions. Irrespective of Prandtl number, the molten pool is hemispheric for small Marangoni number roughly less than 100. In view of negligible Marangoni force, heat transfer in the molten pool is conduction in radial directions. A further increase in Marangoni number results in the bottom of the molten pool to change from hemisphere to convex. As Marangoni number is greater than 10^4–10^5 for Prandtl number greater than 4, the second small cell is induced near the edge of the molten pool. The second cell occurs because of a

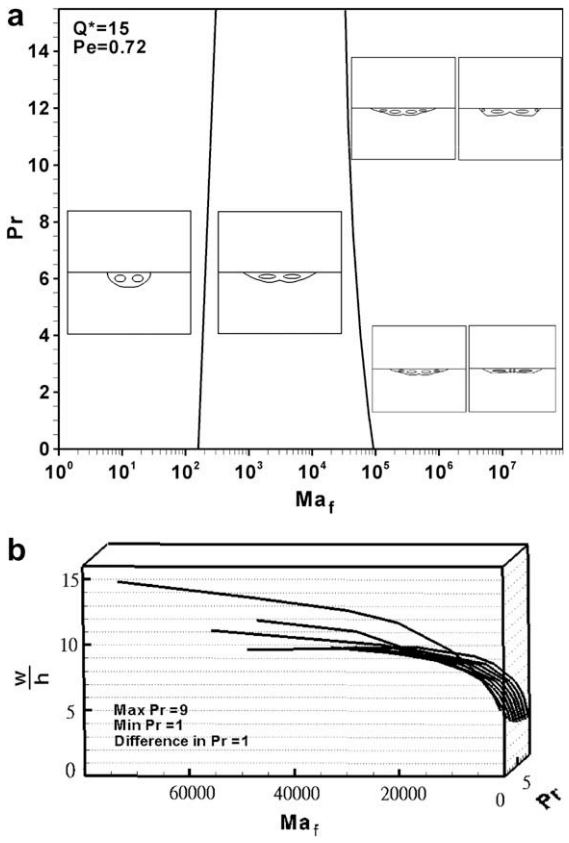

Fig. 3. Dimensionless (a) flow patterns, (b) width-to-depth ratios of molten pools for different Marangoni and Prandtl numbers.

rapid temperature drop near the cold edge. It is interesting to find that the edge of the molten pool is long and thin, resulted from penetration of Marangoni convection, as can be interpreted later. The maximum depth of the molten pool is displaced away from the centerline by increasing Marangoni number. Eventually, the long and thin edge is disappeared and left a small cell near the edge. This leads to slight decrease and increase in the width and depth of the molten pool, respectively. For Prandtl numbers roughly less than 4, a second small cell is induced near the central line of the convex molten pool. This is attributed to the drop of surface temperature near the edge of the incident flux. The flow patterns and molten pool shapes are similar extension from those for Prandtl number less than unity [25].

The corresponding the width-to-depth ratio as a function of Marangoni and Prandtl numbers for Prandtl number greater than unity is shown in Fig. 3(b). The increase in small Marangoni number increases the width-to-depth ratio of the molten pool rapidly from around 2 to the maximum around 14 and 8 for Prandtl numbers less and greater than 5, respectively. This reflects the facts that the molten pool in the hemisphere shape is dominated by heat conduction, and rapidly changed to a shallow shape controlled by Marangoni convection. The effects of Marangoni number on the width-to-depth ratio thus are pronounced for smaller Prandtl numbers. A further increase in Marangoni number gradually reduces the increase of the width-to-depth ratio until asymptotic values are reached.

In order to support description of previous Fig. 3(b), the corresponding dimensionless depths of the molten pool shape for different Marangoni and Prandtl numbers are shown in Fig. 4(a). Except for very small Prandtl numbers of, for example, 0.06, the molten pool depth, which decreases with increasing Marangoni number in a range less than 10^3, is insensitive to the variation of Prandtl number. It is interesting to find that a further increase in Marangoni number results in the molten pool depth to decrease further and then increase. Furthermore, even though the molten pool for $Pr = 9$ has the long and thin edge, the pool depth at the centerline increases with Marangoni number. The deviations between molten pool depths are increased by increasing Marangoni number and difference in Prandtl numbers, where the minimum molten pool depth occurs at $Pr = 1$. Significant increase in the depth with the similar and pronounced trend is found for very low Prandtl numbers. The reason for this is that the secondary cell is induced near the bottom of the pool [25]. Fig. 4(b) shows that the dimensionless molten pool width, which increases with Marangoni number, is nearly independent of Prandtl number for $Pr > 1$. The molten pool width, however, decreases with Prandtl number for $Pr < 1$. As

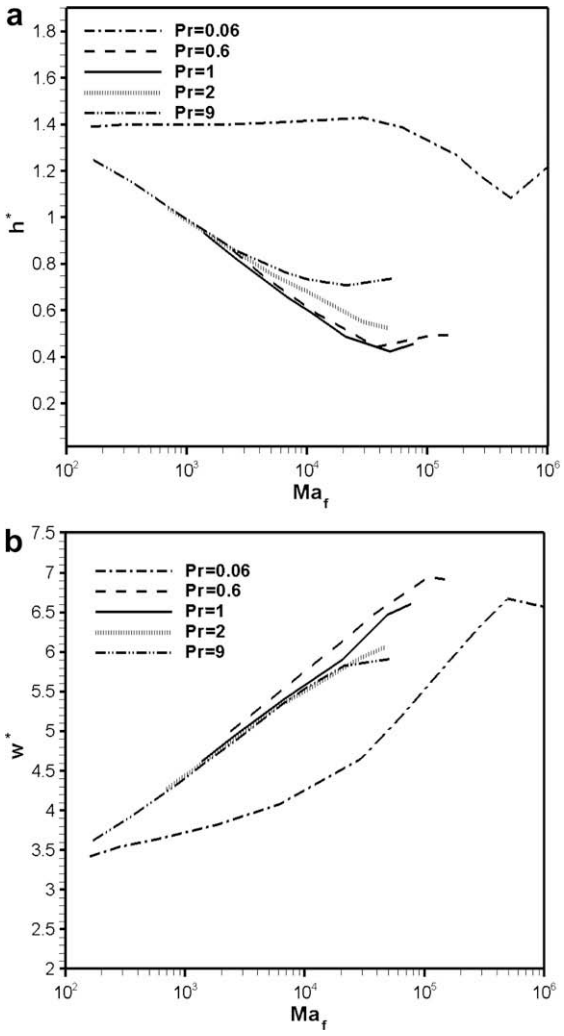

Fig. 4. Dimensionless (a) depths and (b) widths of molten pools for different Marangoni and Prandtl numbers.

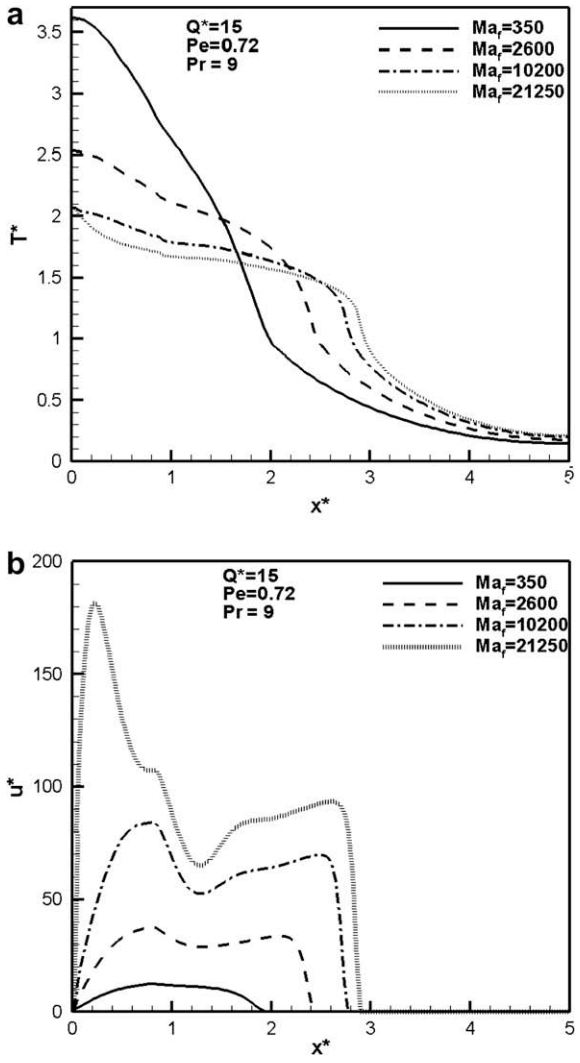

Fig. 5. Computed dimensionless (a) temperature and (b) velocity on free surface corresponding to the maximum molten pool for different Marangoni numbers at $Pr = 9$.

Marangoni number is sufficiently high, an increase in Marangoni number may reduce the molten pool width.

The effects of Marangoni number on the dimensionless temperature profile along the free surface corresponding to previous figures at a Prandtl number of 9 are shown in Fig. 5(a). It can be seen that surface temperature exhibits three distinct regimes, the hot, intermediate and cold corner regimes. Rather than the intermediate regime, curvatures of surface temperature in the hot and cold corner regimes are negative, indicating Marangoni force increases in the outward direction. The hot regime is irradiated by incident flux roughly within $0 \leq x^* \leq 1$. The cold corner regime is near the edge of the pool, where the transition between solid and liquid takes place. In view of enhanced outward and upward flows near the free surface, the width of the intermediate regime is increased, and the resulted surface temperature and its drop in the hot and intermediate regimes are decreased by increasing Marangoni number. On the other hand, an increase in Marangoni number reduces the width and increases surface temperature gradient in the cold corner regime.

The corresponding dimensionless surface speed is shown in Fig. 5(b), indicating the outward flow increases rapidly until the location near beam radius is reached. Surface speed then drops, as a result of the decrease in surface temperature gradient in the intermediate regime. It is noted that the opposite result was found in the case of Prandtl number much less than unity, where surface velocity increases in the intermediate regime until the cold corner regime is reached [25]. A secondary peak is found to take place near the pool edge. The second peak surface velocity is resulted from Marangoni force via the rapid drop of surface temperature in the cold corner regime. Its jump increased with increasing Marangoni number. As Marangoni number becomes as high as

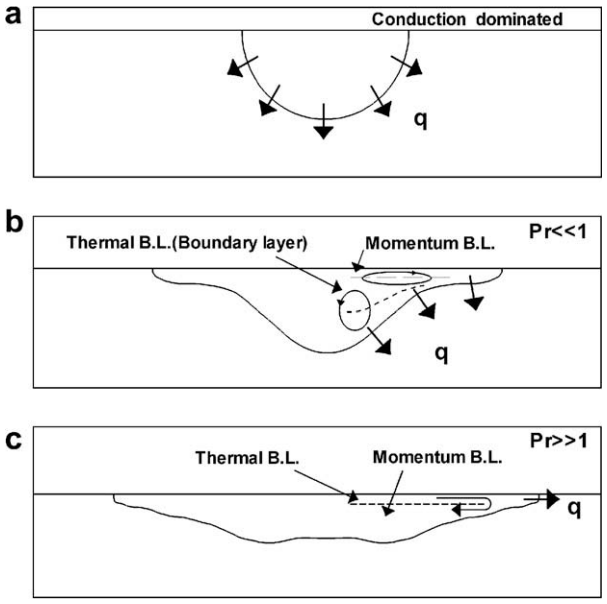

Fig. 7. Sketch for the effects of Prandtl number on molten pool shapes, (a) $Pr \to 0$, (b) $Pr << 1$, and (c) $Pr >> 1$.

2×10^4, the surface temperature and velocity profiles exhibit oscillatory behavior near the centerline. An investigation of the oscillations near the centerline is of interest and challenging.

The computed dimensionless flow and temperature fields and molten pool shapes corresponding to the maximum molten pool for Marangoni number $Ma_f = 10{,}200$ are shown in Fig. 6(a). This fig-

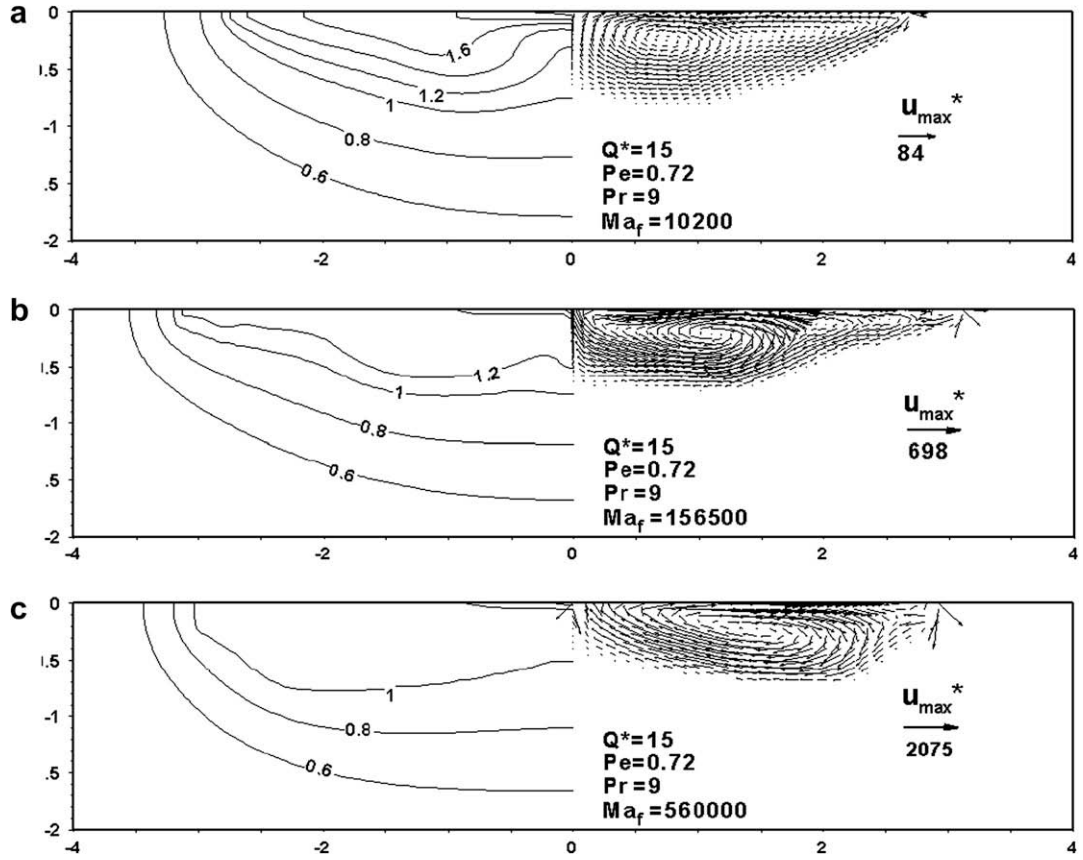

Fig. 6. Computed dimensionless flow and temperature fields corresponding to the maximum molten pool at $Pr = 9$ for (a) $Ma_f = 10{,}200$, (b) $Ma_f = 156{,}500$, and (c) $Ma_f = 560{,}000$.

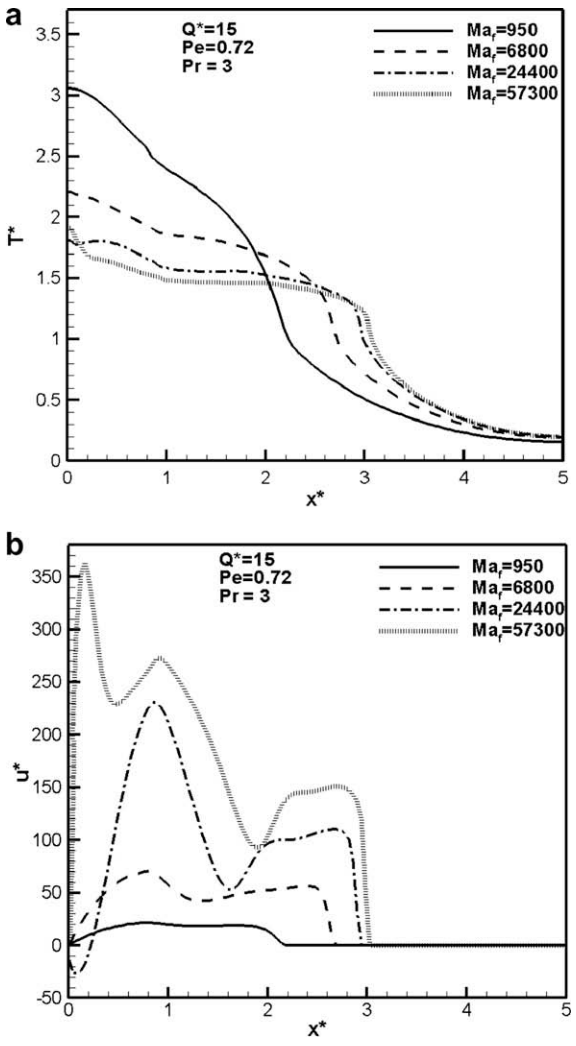

Fig. 8. Computed dimensionless (a) temperature and (b) velocity on free surface corresponding to the maximum molten pool for different Marangoni numbers at $Pr = 3$.

ure demonstrates the flow and temperature fields for a case in previous figures (Fig. 5(a) and (b)). Evidently, the flow forms a vortex cell circulating in the clockwise direction, as shown on the right-hand side, due to a negative surface tension coefficient. The temperature field shown on the left-hand side is distorted owing to thermocapillary convection in the outward direction on the free surface and upward direction along the centerline. The molten pool thus is shallow and the bottom is a convex shape. The half width of the molten pool is greater than the energy distribution parameter of the incident flux primarily due to Marangoni convection. The other small cell rotating in the same clockwise direction also occur near the edge and free surface for a high Marangoni number of 156,500, as shown in Fig. 6(b). It is interesting to find that the shape of the molten pool near the edge is long and thin. The long and thin edge of the molten pool is disappeared for a further increase in Marangoni number, as shown in Fig. 6(c). The maximum depth is further displaced in the outward direction by increasing Marangoni number. It is interesting to find that the isothermals in the molten pool are rather uniform.

To interpret the long and thin edge of the molten pool, a schematic sketch is proposed and shown in Fig. 7(a) through (c). As illustrated in Fig. 7(a), the molten pool shape is a hemisphere for a Prandtl number approaching zero. In this case, thermal diffusion dominates heat transfer. Pure heat conduction in radial directions thus is responsible for the molten pool shape, while directional convective heat transfer is negligible. In the case of Prandtl numbers less than unity, as illustrated in Fig. 7(b), the thickness of the thermal boundary layer is thicker than that of the momentum boundary layer. Heat transfer across the boundary of the molten pool therefore is approximately in radial directions. The bottom of the molten pool shape thus is concave. Fig. 7(c) shows that the thickness of the thermal boundary layer is thinner than that of the momentum boundary layer for Prandtl number greater than unity. Marangoni convection in a thin layer therefore penetrates the solid along the surface and produces a long and thin edge of the molten pool.

A decrease in Prandtl number to $Pr = 3$ for a given Marangoni number results in surface temperature to increase and velocity to decrease, as shown in Fig. 8(a) and (b), respectively. The decrease in surface velocity with Prandtl number is attributed to a decrease

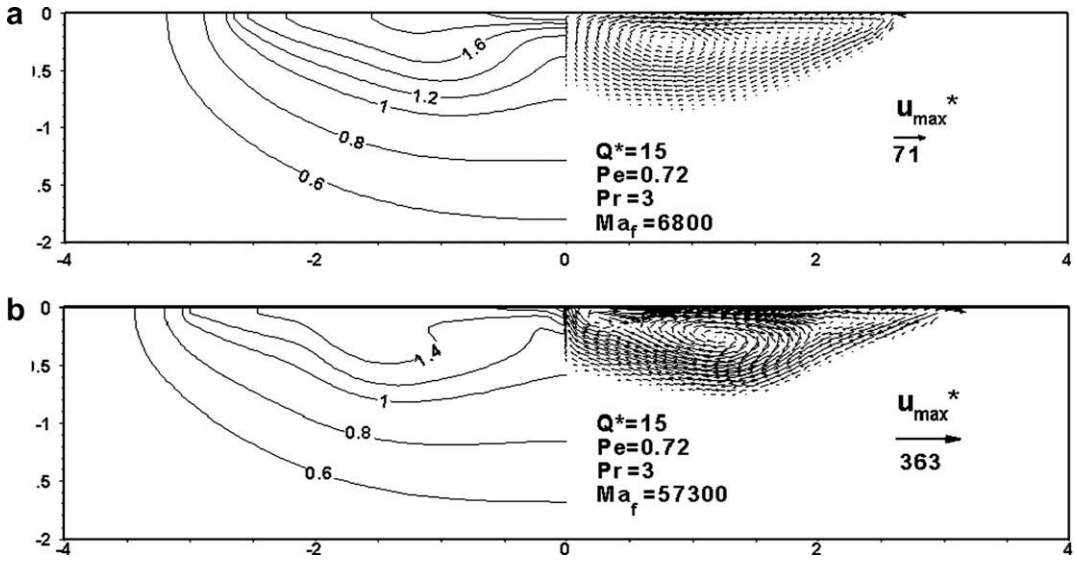

Fig. 9. Computed dimensionless flow and temperature fields corresponding to the maximum molten pool at $Pr = 3$ for (a) $Ma_f = 6800$, (b) $Ma_f = 57{,}300$.

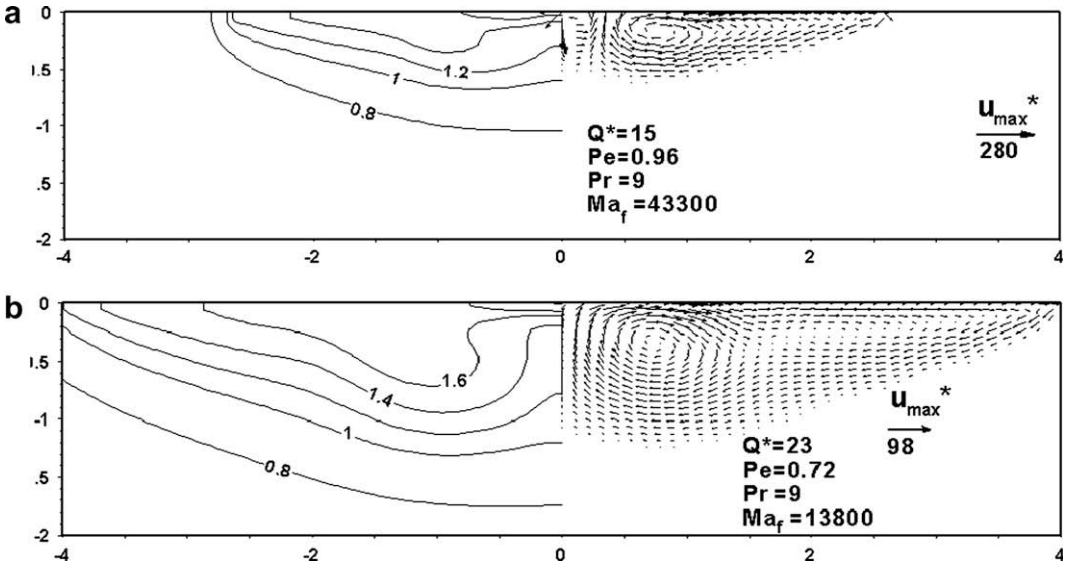

Fig. 10. Computed dimensionless flow and temperature fields corresponding to the maximum molten pool at $Pr = 9$ and for (a) $Ma_f = 43{,}300$ and $Pe = 0.96$, and (b) $Ma_f = 13{,}800$ and $Q^* = 23$.

in viscosity, which reduces surface tension coefficient to maintain the same Marangoni number. Referred to previous Fig. 7(c) in the case of Prandtl number greater than unity, the increase in surface temperature resulted from decreasing Prandtl number can be interpreted by a decrease in surface speed to satisfy energy conservation in the thermal boundary layer whose thickness is less that of momentum boundary layer. On the other hand, for Prandtl number less than unity the increase in surface temperature resulted from a decrease in Prandtl number is due to a decrease in surface velocity and enhanced heat conduction through the momentum boundary layer to the pool bottom in the thick thermal boundary layer. Surface temperature and velocity profiles are quite similar for different Prandtl numbers (see Fig. 5(a) and (b)). Two peaks of surface velocity can be found. The first peak is located near the boundary of the energy beam, while the second peak, which can be a half of the first peak, takes place near the edge of the cold corner regime. Their occurrences are apparently attributed to Marangoni force induced by significant drop of surface temperature. Two peak velocities thus are increased with increasing Marangoni number. The positive curvature of the surface temperature in the intermediate region results in a decrease in surface velocity. The width and depth of separation between two peaks are increased with increasing Marangoni number. The flow patterns and temperature fields corresponding to Marangoni numbers of 6,800 and 57,300 are presented in Fig. 9(a) and (b), respectively.

The effects of Peclet number on temperature fields and molten pool shapes are shown in Fig. 10(a). An increase in Peclet number results in decreases in velocity and temperature and molten pool sizes. This is because for an increase in Peclet number implies a decrease in incident energy per unit welding length to heat and melt the incoming solid, as can be seen from the energy balance $Q \sim \rho U w h[c_p(T_m - T_\infty) + h_{s\ell}]$. Flow patterns, temperature fields and the molten pool shapes with a long and thin edge are similar to previous Fig. 6(b). Referring to previous Fig. 6(a) and (b), Fig. 10(b) show that an increase in dimensionless beam power evidently increases the width and depth of the molten pool, while fluid flow and temperature fields are similar. The long and thin edge is enhanced by increasing beam power. These figures implies the flow patterns and width-to-depth ratios induced by changing Peclet number and dimensionless beam power are similar to those presented in previous Fig. 3(a) and (b).

4. Conclusions

The following are the main conclusions:

1. The molten pool shapes for Prandtl number greater than unity exhibit distinct regions: (i) The pool shape is a hemisphere for Marangoni number $Ma_f < 100$; (ii) The pool bottom becomes convex for $100 < Ma_f < 10^5$; (iii) The bottom of the shallow pool is slightly convex near the centerline for $Pr < 4$ and $Ma > 10^5$; (iv) The pool penetrates along the top surface, resulting in a long and thin edge for $Pr > 4$ and $Ma_f > 10^5$. This edge is disappeared as Marangoni number further increases.
2. The long and thin edge is a result of the thickness of thermal boundary layer less than that of momentum boundary layer. Melting occurs by penetrative heating from thin thickness of thermal boundary layer.
3. Except for very small Prandtl numbers (for example, $Pr = 0.06$), the decrease in the pool depth with increasing Marangoni number in a range less than 10^3 is insensitive to the variation of Prandtl number. A further increase in Marangoni number results in the pool depth to continuously decrease and then increase. The deviation of pool depths is increased by increasing Marangoni number and difference in Prandtl numbers, where the minimum pool depth occurs at $Pr = 1$. Significant increase in the depth with the similar and pronounced trend is found for very low Prandtl numbers.
4. The pool width, which increases with Marangoni number, is nearly independent of Prandtl number for $Pr > 1$. The pool width, however, decreases with Prandtl number for $Pr < 1$. As Marangoni number is sufficiently high, an increase in Marangoni number may reduce the pool width.
5. The width-to-depth ratio of the pool exhibits a rapid increase by increasing small Marangoni number, irrespective of Prandtl number. The minimum width-to-depth around 2 reflects a hemispherical molten pool, dominated by pure conduction. The subsequent increase in the width-to-depth ratio is attributed to Marangoni convection. As Marangoni number further increases, the increase of the width-to-depth ratio reduces. For given Marangoni number

the width-to-depth ratio decreases with increasing Prandtl number.

6. The surface temperature reveals the hot, intermediate and cold corner regions. The hot region is irradiated by incident flux, whereas the cold corner region is near the edge of the pool. Surface temperatures in the hot and cold corner regions exhibit significant drop. As Marangoni and Prandtl numbers increase, widths of the intermediate and cold corner regions increase and decrease, respectively.
7. Surface temperature in the hot region is decreased with increasing Prandtl and Marangoni numbers. The curvature of surface temperature in the cold corner region is more negative by reducing Prandtl number.
8. In the case of $Pr > 1$ the increase in surface temperature resulted from decreasing Prandtl number can be interpreted by a decrease in surface speed to satisfy energy conservation in the thermal boundary layer whose thickness is less that of momentum boundary layer. On the other hand, for $Pr < 1$ the increase in surface temperature from a decrease in Prandtl number is due to a decrease in surface velocity and enhanced heat conduction through the momentum boundary layer to the pool bottom in the thick thermal boundary layer.
9. The first peak of surface velocity is located near the boundary of the energy beam, whereas the second peak, which can be a half of the first peak, takes place near the edge of the cold corner region. Their occurrences are attributed to Marangoni force induced by significant drop of surface temperature. Two peak velocities thus are increased with increasing Marangoni number.
10. The positive curvature of the surface temperature in the intermediate region results in a decrease in surface velocity. The width and depth of separation between two peaks are increased with increasing Marangoni number.
11. As Marangoni number is greater than 2×10^4, surface velocity and temperature becomes oscillatory near the centerline.
12. Irrespective of Prandtl number, the peak surface temperature is increased with decreasing Peclet number or scanning speed of the incident flux, and increasing dimensionless beam power. The flow and temperature fields, however, are similar.

References

[1] S. Kou, Welding Metallurgy, Wiley, New York, 1987.
[2] S.A. David, T. DebRoy, Current issues and problems in welding science, Science 257 (1992) 497–502.
[3] T. Zacharia, J.M. Vitek, J.A. Goldak, T. DebRoy, M. Rappaz, H.K.D.H. Bhadeshia, Modeling of fundamental phenomena in welds, Modell. Simul. Mater. Sci. Eng. 3 (1995) 265–288.
[4] K. Mundra, T. DebRoy, S.S. Babu, S.A. David, Weld metal microstructure calculations from fundamentals of transport phenomena in the arc welding of low-alloy steels, Welding J. 76 (1997) 163-s–171-s.
[5] W. Liu, J.N. DuPont, Effects of melt-pool geometry on crystal growth and microstructure development in laser surface-melted superalloy single crystals. Mathematical modeling of single-crystal growth in a melt pool (part I), Acta Mater. 52 (2004) 4833–4847.
[6] S. Kou, Y.H. Wang, Weld pool convection and its effect, Welding J. 65 (1986) 63-s–70-s.
[7] B. Basu, A.W. Date, Numerical study of steady state and transient laser melting problems-I: characteristics of flow field and heat transfer, Int. J. Heat Mass Transfer 33 (1990) 1149–1163.
[8] M. Kanouff, R. Greif, The unsteady development of a GTA weld pool, Int. J. Heat Mass Transfer 35 (1992) 967–979.
[9] T. Zacharia, S.A. David, J.M. Vitek, T. DebRoy, Weld pool development during GTA and laser beam welding of type 304 stainless steel, part I – theoretical analysis, Welding J. 68 (1989) 499-s–509-s.
[10] C. Chan, J. Mazumder, M.M. Chen, A two-dimensional transient model for convection in laser melted pools, Metall. Trans. 15A (1984) 2175–2184.
[11] A. Paul, T. DebRoy, Free surface flow and heat transfer in conduction mode laser welding, Metall. Trans. 19B (1988) 851–858.
[12] K. Mundra, T. DebRoy, Toward understanding alloying element vaporization during laser beam welding of stainless steel, Welding J. 72 (1993) 1-s–9-s.
[13] P.S. Wei, C.Y. Chang, C.T. Chen, Surface ripple in electron-beam welding solidification, J. Heat Transfer 118 (1996) 960–969.
[14] U. Gratzke, P.D. Kapadia, J. Dowden, J. Kroos, G. Simon, Theoretical approach to the humping phenomenon in welding processes, J. Phys. D: Appl. Phys. 25 (1992) 1640–1647.
[15] P.F. Mendez, T.W. Eagar, Penetration and defect formation in high-current arc welding, Welding J. 82 (2003) 296-s–306-s.
[16] A. Kumar, T. DebRoy, Toward a unified model to prevent humping defects in gas tungsten arc welding, Welding J. 85 (2006) 292-s–304-s.
[17] H. Tong, W.H. Giedt, A dynamic interpretation of electron beam welding, Welding J. 49 (1970) 259-s–266-s.
[18] D.A. Schauer, W.H. Giedt, Prediction of electron beam welding spiking tendency, Welding J. 57 (1978) 189-s–195-s.
[19] W.H. Giedt, A periodic melting model of high intensity electron beam welding, in: M. Rappaz, M.R. Özgü, K.W. Mahin, (Eds.), Proceedings of the 5th International Conference on Modeling of Casting, Welding, and Advanced Solidification Processes-V, Davos, Switzerland, September 16–21, TMMMS, Warrendale, PA, 1991, pp. 115–122.
[20] P.S. Wei, Y.K. Kuo, S.H. Chiu, C.Y. Ho, Shape of a pore trapped in solid during solidification, Int. J. Heat Mass Transfer 43 (2000) 263–280.
[21] C.R. Heiple, J.R. Roper, Mechanism for minor element effect on GTA fusion zone geometry, Welding J. 61 (1982) 97-s–102-s.
[22] C. Limmaneevichitr, S. Kou, Experiments to simulate effect of Marangoni convection on weld pool shape, Welding J. 79 (2000) 231-s–237-s.
[23] F.K. Chung, P.S. Wei, Mass, momentum, and energy transport in a molten pool when welding dissimilar metals, J. Heat Transfer 121 (1999) 451–461.
[24] P.S. Wei, F.K. Chung, Unsteady Marangoni flow in a molten pool when welding dissimilar metals, Metall. Mater. Trans. B 31B (2000) 1387–1403.
[25] P.S. Wei, C.N. Ting, J.S. Yeh, T. DebRoy, F.K. Chung, G.H. Yan, Origin of wavy weld boundary, J. Appl. Phys. 105 (2009) 053508-1–053508-8.
[26] G.K. Hicken, W.H. Giedt, A.E. Bentley, Correlation of joint penetration with electron beam current distribution, Welding J. 70 (1991) 69-s–75-s.
[27] P. Burgardt, Electron beam beam size calibration, in: L.N. Tallerico, (Eds.), Summary of Calibration of Welding Systems Meeting, Sandia National Lab., Livermore, CA, 1986, pp. 258–266.
[28] A.K. Sen, S.H. Davis, Steady thermocapillary flows in two-dimensional slots, J. Fluid Mech. 121 (1982) 163–186.
[29] M. Salcudean, M. Choi, R. Greif, A study of heat transfer during arc welding, Int. J. Heat Mass Transfer 29 (1986) 215–225.
[30] S. Ostrach, Low-gravity fluid flows, Annu. Rev. Fluid Mech. 14 (1982) 313–345.
[31] M.M. Chen, Thermocapillary convection in materials processing, in: S.K. Samanta, R. Komanduri, R. McMeeking, M.M. Chen, A. Tseng (Eds.), Interdisciplinary Issues in Materials Processing and Manufacturing, ASME, New York, 1987, pp. 541–558.
[32] D. Rivas, S. Ostrach, Scaling of low-Prandtl-number thermocapillary flows, Int. J. Heat Mass Transfer 35 (1992) 1469–1479.
[33] T. Zacharia, S.A. David, J.M. Vitek, T. DebRoy, Weld pool development during GTA and laser beam welding of type 304 stainless steel, part II – experimental correlation, Welding J. 68 (1989) 510-s–519-s.
[34] K. Mundra, T. DebRoy, T. Zacharia, S.A. David, Role of thermophysical properties in weld pool modeling, Welding J. 71 (1992) 313-s–320-s.
[35] W. Pitscheneder, T. DebRoy, K. Mundra, R. Ebner, Role of sulfur and processing variables on the temporal evolution of weld pool geometry during multikilowatt laser beam welding of steels, Welding J. 75 (1996) 71-s–80-s.